Does the Fundamental Metallicity Relation evolve with redshift? A perspective from cosmological simulations

Alex M. Garcia[1★], Paul Torrey[1], Sara Ellison[2], Kathryn Grasha[4,5,6†], Lars Hernquist[3], Henry R.M. Zovaro[4,5], Qian-Hui Chen[4,5], Lisa J. Kewley[3], Erica J. Nelson[7], Z.S. Hemler[8]
[1]*Department of Astronomy, University of Virginia, Charlottesville, VA 22904, USA*
[2]*Department of Physics & Astronomy, University of Victoria, Finnerty Road, Victoria, British Columbia, V8P 1A1, Canada*
[3]*Institute for Theory and Computation, Harvard-Smithsonian Center for Astrophysics, Cambridge, MA 02138, USA*
[4]*Research School of Astronomy & Astrophysics, Australian National University, Canberra, Australia, 2611*
[5]*ARC Centre of Excellence for All Sky Astrophysics in 3 Dimensions (ASTRO 3D), Australia*
[6]*Visiting Fellow, Harvard-Smithsonian Center for Astrophysics, 60 Garden Street, Cambridge, MA 02138, USA*
[7]*Department for Astrophysical and Planetary Science, University of Colorado, Boulder, CO 80309, USA*
[8]*Department of Astrophysical Sciences, Princeton University, Peyton Hall, Princeton, NJ, 08544, USA*

Accepted XXX. Received YYY; in original form ZZZ

ABSTRACT

The scatter about the mass metallicity relation (MZR) has a correlation with the gas content of systems (indicated by, e.g., gas fraction or star formation rate). The lack of evidence of evolution in the correlated scatter at $z \lesssim 2.5$ leads many to refer to the relationship between mass, metallicity, and SFR as the Fundamental Metallicity Relation (FMR). Yet, recent high-redshift ($z > 3$) *JWST* observations have challenged the fundamental nature of the FMR. In this work, we show that the cosmological simulations Illustris, IllustrisTNG, and EAGLE all predict non-negligible evolution in the strength of the MZR's secondary correlation with SFR as a function of redshift. We find that the scatter can be decreased by an additional 10-30% at $z \gtrsim 4$ when examining individual redshifts compared to fitting all redshifts together, further suggesting FMR evolution.

Key words: galaxies: high-redshift – galaxies: abundances – galaxies: evolution

1 INTRODUCTION

The metal content of galaxies provides key insights into galaxy evolution. Stellar winds and supernovae explosions eject metals formed in stars into the interstellar medium (ISM). Metals then mix via galactic winds (e.g., Lacey & Fall 1985; Koeppen 1994) and turbulence (e.g., Elmegreen 1999) within the disc while pristine gas accretion from the circumgalactic medium (CGM) and outflows dilute the metal content (e.g., Somerville & Davé 2015). Thus, the metal content (metallicity) of the gas within a galaxy is sensitive to such processes, providing a window into the evolutionary processes within a galaxy (Dalcanton 2007; Kewley et al. 2019).

Evidence for the sensitivity of metal content to the gas dynamics within a galaxy is perhaps most clearly seen within the relationship between the stellar mass of a galaxy and its gas-phase metallicity. This mass-metallicity relationship (MZR) describes a relationship of increasing metal content in galaxies with increasing stellar mass (Tremonti et al. 2004; Lee et al. 2006). At low stellar masses, the MZR relationship is well-described as a power-law, whereas at high masses ($\log[M_*/M_\odot] > 10.5$) the MZR plateaus (e.g., Tremonti et al. 2004; Zahid et al. 2014; Blanc et al. 2019). Furthermore, at a fixed stellar mass, low (high) metallicity galaxies have systematically elevated (depressed) gas content (indicated by, e.g., gas fraction, star formation rate, or molecular gas mass; Ellison et al. 2008; Mannucci et al. 2010; Bothwell et al. 2013). The inverse relationship between a galaxy's metal and gas content at a fixed stellar mass has been seen in the gas-phase in observations (e.g., Lara-López et al. 2010; Bothwell et al. 2016; Yang et al. 2024) and simulations (e.g., De Rossi et al. 2017; Torrey et al. 2018) as well as for stellar metallicities in simulations (De Rossi et al. 2018; Fontanot et al. 2021; Garcia et al. 2024; Looser et al. 2024) and recent observations (Looser et al. 2024). This secondary dependence on gas content is qualitatively well-described with basic competing physical drivers: (i) as new pristine gas is accreted onto a galaxy, it drives galaxies toward higher gas fractions, higher star formation rates (SFRs), and lower metallicities, while (ii) galaxies will persistently tend to consume gas and produce new metals, driving galaxies toward lower gas fractions, lower SFRs, and higher metallicities (e.g., Davé et al. 2011; Dayal et al. 2013; Lilly et al. 2013; De Rossi et al. 2015; Torrey et al. 2018). It is therefore expected that secondary dependence would remain present for galaxies across a wide redshift range given the ubiquity of these physical drivers.

At higher redshift the MZR has been seen to persist (albeit with a lowered overall normalisation e.g., Savaglio et al. 2005; Maiolino et al. 2008; Zahid et al. 2011; Langeroodi et al. 2023) along with the secondary dependence on gas content (e.g., Belli et al. 2013; Salim et al. 2015; Sanders et al. 2018, 2021). Critically, it has been put forth

★ E-mail: alexgarcia@virginia.edu
† ARC DECRA Fellow

that a single, redshift-invariant plane can be used to describe both the general evolution of the MZR as well as the secondary correlations (Mannucci et al. 2010). This single surface/relation that can describe the metallicity of galaxies over a wide mass and redshift range is referred to as the fundamental metallicity relation (FMR) – where its "fundamental" nature is usually tied to its redshift invariance. Recently, however, *JWST* observations have challenged the claim that the FMR can describe galaxies at $z > 3$ (Heintz et al. 2023; Curti et al. 2023; Langeroodi & Hjorth 2023; Nakajima et al. 2023).

The core challenge of the FMR is that it aims to characterise two distinct features of the MZR at the same time: (i) the secondary relationship with gas content at fixed redshift, and (ii) the redshift evolution of the normalisation. It is therefore possible that a change in either the strength of the MZR's secondary correlation with SFR or the overall redshift evolution of the normalisation of the MZR (or perhaps a combination thereof) might indicate FMR evolution. Many studies to this point focus solely on applying a $z \sim 0$ fit to higher redshift data (e.g., Mannucci et al. 2010; Wuyts et al. 2012; Belli et al. 2013; Sanders et al. 2021; Curti et al. 2023; Langeroodi & Hjorth 2023; Nakajima et al. 2023). It is unclear how to effectively decouple (and subsequently interpret) any potential evolution in either the scatter about the MZR or the evolution of the normalisation (or a combination thereof) in these frameworks. Some work has been done up to this point observationally looking at higher redshifts independently to specifically isolate the scatter about the MZR (e.g., Salim et al. 2015; Sanders et al. 2015, 2018; Pistis et al. 2023). These works find that there may be some evolution within the scatter about the MZR at intermediate redshifts (Pistis et al. 2023 suggest potentially as low at $z \sim 0.63$). Yet, there are comparatively few simulations results on a systematic examinations on the strength of the secondary dependence on gas content and/or SFR at individual redshifts.

In this work, we demonstrate the evolution of the MZR's secondary dependence on SFR from the perspective of the cosmological simulations Illustris, IllustrisTNG, and EAGLE. The rest of the paper is as follows: In §2 we describe the simulations we use, our galaxy selection criteria, and summarize definitions of the FMR. In §3 we present the redshift evolution of the FMR as found in simulations. In §4 we quantify the impact of the new framework on the scatter about the MZR, discuss the advantages and challenges in the new framework, and then discuss potential impacts of the physical models. Finally, in §5 we present our conclusions.

2 METHODS

We use the Illustris, IllustrisTNG, and EAGLE cosmological simulations to investigate the dependence of the gas-phase metallicity on stellar mass and star formation. Each of these simulations has a sub-grid ISM pressurisation model, which creates "smooth" stellar feedback. We believe that generic results from all three of these simulations should constitute a fair sampling of predictions from sub-grid ISM pressurisation models owing to the appreciably different physical implementations.

Here we briefly describe each of the simulations from this analysis, the galaxy selection criteria we employ, and present a new framework for interpreting the Mannucci et al. (2010; hereafter M10) FMR projection. All measurements are reported in physical units.

2.1 Illustris

The original Illustris suite of cosmological simulations (Vogelsberger et al. 2013, 2014a,b; Genel et al. 2014; Torrey et al. 2014) was run with the moving-mesh code AREPO (Springel 2010). The Illustris model accounts for many important astrophysical processes, including gravity, hydrodynamics, star formation/stellar evolution, chemical enrichment, radiative cooling and heating of the ISM, stellar feedback, black hole growth, and AGN feedback. The unresolved star forming ISM uses the Springel & Hernquist (2003; hereafter, SH03) equation of state, wherein new star particles are created from regions of dense ($n_{\rm H} > 0.13$ cm^{-3}) gas. The masses of the stars within the star particle are drawn from a Chabrier (2003) initial mass function (IMF) and metallicities are adopted from the ISM where they are born. As the stars evolve, they eventually return their mass and metals back into the ISM. The stellar mass return and yields used allow for the direct simulation of time-dependent return and heavy metal enrichment, explicitly tracking nine different chemical species (H, He, C, N, O, Ne, Mg, Si, and Fe).

The Illustris suite consists of a single volume of size (106.5 Mpc)^3 at three different resolutions. The three resolutions are as follows: Illustris-1 (2×1820^3 particles), Illustris-2 (2×910^3 particles), and Illustris-3 (2×455^3 particles). We use Illustris-1, the highest resolution run, which is hereafter we refer to synonymously with Illustris itself.

2.2 IllustrisTNG

IllustrisTNG (The Next Generation; Marinacci et al. 2018; Naiman et al. 2018; Nelson et al. 2018; Pillepich et al. 2018b; Springel et al. 2018; Pillepich et al. 2019; Nelson et al. 2019a,b, hereafter TNG) is the successor to the original Illustris simulations, alleviating some of the deficiencies of and updating the original Illustris model. As such, the Illustris and TNG models are similar, yet have an appreciably different physical implementation (see Weinberger et al. 2017; Pillepich et al. 2018a, for a complete list of differences between the models). TNG implements the same equation of state for the dense star forming ISM as Illustris (SH03). Furthermore, TNG tracks the same nine chemical species as Illustris, while also following a tenth "other metals" as a proxy for metals not explicitly monitored.

TNG consists of three different volumes each with their own sub-resolution runs: TNG50 (51.7 Mpc)^3, TNG100 (110.7 Mpc)^3, and TNG300 (302.6 Mpc)^3. In this work, we will use the highest resolution TNG100 run (TNG100-1; hereafter used synonymously with TNG), with 2×1820^3 particles, as a comparable volume and resolution to the original Illustris.

2.3 EAGLE

Unlike Illustris and TNG, "Evolution and Assembly of GaLaxies and their Environment" (EAGLE, Crain et al. 2015; Schaye et al. 2015; McAlpine et al. 2016) employs a heavily modified version of the smoothed particle hydrodynamics (SPH) code GADGET-3 (Springel 2005; ANARCHY, see Schaye et al. 2015 Appendix A). EAGLE includes many of the same baryonic processes (star-formation, chemical enrichment, radiative cooling and heating, etc) as Illustris and TNG. The dense (unresolved) ISM in EAGLE is also treated with a sub-grid equation of state (Schaye & Dalla Vecchia 2008; hereafter, SDV08), much like that of SH03. The SDV08 prescription forms stars according to a Chabrier (2003) IMF from the dense ISM gas. The density threshold for star formation is given by the metallicity-dependent transition from atomic to molecular gas computed by

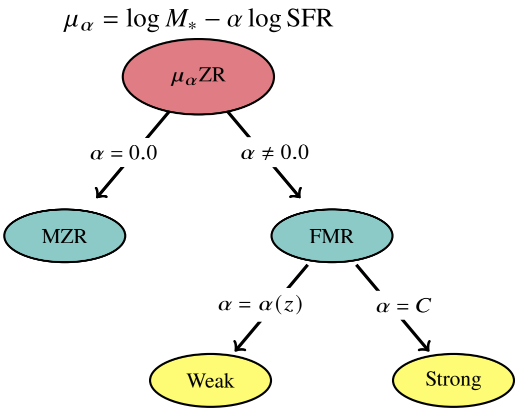

Figure 1. Decision tree for the μ_αZR, see Section 2.5 for full details. This shows the different relationships that can be included under the umbrella μ_α metallicity relation (μ_αZR; see Equation 1). First is the traditional MZR where $\alpha = 0.0$ and second is the FMR where $\alpha \neq 0.0$. The FMR can be further broken into two categories: strong and weak depending on if α varies as a function of redshift (weak) or not (strong).

Schaye (2004). Stellar populations evolve according to the Wiersma et al. (2009) evolutionary model and eventually return their mass and metals back into the ISM. EAGLE explicitly tracks eleven different chemical species (H, He, C, N, O, Ne, Mg, Si, S, Ca, and Fe).

The full EAGLE suite is comprised of several simulations ranging from size (25 Mpc)^3 to (100 Mpc)^3. We use data products at an intermediate resolution (2×1504^3 particles) run with a box-size of (100 Mpc)^3 referred to as RefL0100N1504 (hereafter simply EAGLE) as a fair comparison to the selected Illustris and TNG runs.

2.4 Galaxy Selection

All three simulations in this work select gravitationally-bound substructures using subfind (Springel et al. 2001; Dolag et al. 2009), which identifies self-bound collections of particles from within friends-of-friends groups (Davis et al. 1985). We limit our analysis to central galaxies that we consider 'well-resolved' (i.e., containing ∼100 star particles and ∼500 gas particles), thus we restrict the sample to galaxies with stellar mass $\log(M_*\ [M_\odot]) > 8.0$ and gas mass $\log(M_{\rm gas}\ [M_\odot]) > 8.5$. We place an upper stellar mass limit of $\log(M_*\ [M_\odot]) > 12.0$[1]. Following from a number of previous works (see, e.g., Donnari et al. 2019; Nelson et al. 2021; Hemler et al. 2021; Garcia et al. 2023), we exclude quiescent galaxies by defining a specific star formation main sequence (sSFMS). We do so by fitting a linear-least squares regression to the median sSFR-M_* relation with stellar mass $\log(M_*\ [M_\odot]) < 10.2$ in mass bins of 0.2 dex. The sSFMS above $10.2 \log M_\odot$ is extrapolated from the regression. Galaxies that fall greater than 0.5 dex below the sSFMS are not included in our sample. As we show in Garcia et al. (2024; that paper's Appendix B), our key results (using stellar metallicities) are *not* sensitive to our sample selection. We obtain the same result here in the gas-phase: our key results are qualitatively unchanged by the same variations as Garcia et al. (2024) in selection criteria (see Appendix A).

[1] For most redshifts analysed in this work this upper mass limit does not exclude any galaxies

2.5 Definitions of the FMR

M10 propose that the 3D relationship between stellar mass, gas-phase metallicity, and star formation rate (SFR) can be projected into 2D using a linear combination of the stellar mass and star formation:

$$\mu_\alpha = \log M_* - \alpha \log \mathrm{SFR}\,, \tag{1}$$

where α is a free parameter that ranges from 0 to 1[2]. The free parameter α holds all the diagnostic power on the strength of the MZR's secondary dependence with SFR. By varying α, the distribution of galaxies in μ_α-metallicity space varies. We define a μ_α-metallicity relation (μ_αZR) for each α as a linear-least squares regression[3] of the data. We compute the μ_αZR for $\alpha = 0.0$ to 1.0 in steps of 0.01 and obtain the residuals about each regression. The projection that yields the minimum scatter in the residuals (smallest standard deviation) is deemed the best fit. The α value associated with this minimum scatter projection is henceforth referred to as $\alpha_{\rm min}$. We define an uncertainty on $\alpha_{\rm min}$ by assuming that a projection that has scatter within 5% of the minimum value is a plausible candidate for the true $\alpha_{\rm min}$ (following from Garcia et al. 2024).

$\alpha_{\rm min}$ physically represents the direction to project the 3D mass-metallicity-SFR ($M_* - Z_{\rm gas} - \mathrm{SFR}$) space into a minimum scatter distribution in 2D $\mu_\alpha - Z$ space. The central question of an FMR investigation in the M10 framework is "Can the 2D projection explain both: (i) the scatter about the MZR, and (ii) the evolution of normalisation in the MZR through time." Thus, the μ_αZR is the relation of merit in the 2D projection of the $M_* - Z_{\rm gas} - \mathrm{SFR}$ relation. There are two of outcomes, either (i) $\alpha_{\rm min} = 0.0$, wherein the canonical MZR is recovered, or (ii) $\alpha_{\rm min} \neq 0.0$, wherein an FMR is recovered. In this way, the μ_αZR can be thought of as a superset of relations containing the MZR, the strong FMR, and the weak FMR (relationships illustrated in Figure 1). Framing the FMR in this way underscores the decisions required in establishing the FMR. Previous studies have been somewhat restrictive in regards to these decisions. We therefore highlight the need to take a deliberate approach to our definitions to build a framework by which potential redshift evolution can be assessed.

Traditionally (as in, e.g., M10), the FMR is defined by determining $\alpha_{\rm min}$ at $z = 0$. At $z \lesssim 2.5$ this value has been seen to be roughly constant. We henceforth refer to the idea that $\alpha_{\rm min}$ does not vary as a function of redshift as the "strong FMR hypothesis" and the resultant FMR as the "strong FMR". A single $\alpha_{\rm min}$ can describe both the MZR's secondary dependence and its normalisation evolution in the strong FMR. In this work, we investigate the claim that $\alpha_{\rm min}$ is constant over time by identifying the $\alpha_{\rm min}$ value that minimizes scatter at each redshift independently. This procedure allows $\alpha_{\rm min}$ to (potentially) vary as a function of redshift. Here we introduce the concept of a "weak" FMR. We define the weak FMR hypothesis as a counterpoint to the strong FMR hypothesis: $\alpha_{\rm min}$ is *not* constant as a function of redshift.

There are actually more parameters beyond $\alpha_{\rm min}$ that the FMR is defined by: the parameters of the regression (in our case slope

[2] Models exist with more complexity; for example, Curti et al. (2020) introduce a functional form for the FMR (opposed to a 2D projection). We opt to not present other forms of the FMR in this work as a exercise on the extent to which the M10 projection can describe the of scatter at fixed redshift.

[3] M10 use a fourth-order polynomial for fitting. This practice is inconsistent in the literature with many (e.g., Andrews & Martini 2013) considering a linear regression. We show that using a fourth-order polynomial instead of a linear regression does not significantly alter our $\alpha_{\rm min}$ determination in Appendix B.

	Illustris	TNG	EAGLE
$z = 0$	$0.23^{0.34}_{0.08}$	$0.31^{0.59}_{0.00}$	$0.74^{0.86}_{0.57}$
$z = 1$	$0.33^{0.46}_{0.11}$	$0.61^{0.69}_{0.47}$	$0.73^{0.81}_{0.63}$
$z = 2$	$0.39^{0.52}_{0.20}$	$0.60^{0.67}_{0.47}$	$0.65^{0.75}_{0.52}$
$z = 3$	$0.45^{0.56}_{0.30}$	$0.65^{0.72}_{0.55}$	$0.59^{0.68}_{0.44}$
$z = 4$	$0.49^{0.59}_{0.36}$	$0.68^{0.75}_{0.57}$	$0.53^{0.62}_{0.39}$
$z = 5$	$0.52^{0.61}_{0.39}$	$0.70^{0.77}_{0.59}$	$0.46^{0.56}_{0.33}$
$z = 6$	$0.53^{0.63}_{0.39}$	$0.70^{0.77}_{0.59}$	$0.44^{0.54}_{0.31}$
$z = 7$	$0.56^{0.65}_{0.42}$	$0.70^{0.78}_{0.58}$	$0.40^{0.49}_{0.27}$
$z = 8$	$0.59^{0.69}_{0.47}$	$0.70^{0.78}_{0.58}$	$0.31^{0.42}_{0.16}$

Table 1. All $\alpha_{\rm min}$ values at $z = 0-8$ for Illustris, TNG, and EAGLE. These $\alpha_{\rm min}$ values are determined at each redshift individually. The superscripts are the upper limits of the uncertainty while the subscripts are the lower limits. We show these values in Figure 2.

and intercept). These additional parameters add complexity to the interpretation of the evolution. Regressions are inherently linked to the $\alpha_{\rm min}$ determination, yet the parameters of the fit can have a profound impact on interpretation of FMR evolution irrespective of $\alpha_{\rm min}$ variations. The impact of these parameters is beyond the scope of this work since we only examine each redshift bin independently here and the effect of the regression parameters is only felt when comparing different redshift bins. We do, however, address the impact of these parameters in a companion work (Garcia et al. in prep).

3 RESULTS

3.1 Does $\alpha_{\rm min}$ vary as a function of redshift?

We use the best-fit $\alpha_{\rm min}$ values derived as a function of redshift to evaluate whether the scatter about the MZR evolves significantly with redshift. The weak FMR hypothesis is well suited for this purpose because it fits each redshift independently, and is therefore not sensitive to the influence of redshift evolution of the normalisation of the MZR.

We obtain $\alpha_{\rm min}$ values at $z = 0 - 8$ for all three simulations (shown in Figure 2; values presented in Table 1). Uncertainties on $\alpha_{\rm min}$ correspond to the uncertainty in the minimum dispersion (see Section 2.5 for definition). $\alpha_{\rm min}$ values show some level of redshift evolution in all three simulations as can be seen from Figure 2. Interestingly, each simulation has qualitatively different behaviour. TNG $\alpha_{\rm min}$ values vary significantly from $z = 0$ to $z = 1$ but then level off past redshift two, the Illustris $\alpha_{\rm min}$ values increase monotonically with redshift, and the EAGLE values decrease monotonically as a function of redshift.

The evolution in $\alpha_{\rm min}$ implies that the strong FMR hypothesis is not satisfied in any of the three simulations. Redshift evolution of the derived $\alpha_{\rm min}$ values may be indicative of evolution in the driving forces of the scatter about MZR (potentially ramping up or down with time in the case of Illustris and EAGLE). For example, barring $z = 0$, all $\alpha_{\rm min}$ values from TNG agree within uncertainty. As was shown in Garcia et al. (2024), a M_*–Z_*–SFR[4] relation is not apparent at low mass in TNG at $z = 0$. Garcia et al. (2024) attribute this lack of a relationship at $z = 0$ in TNG to the redshift scaling of winds within the TNG model. Briefly, the effect of adding winds that change with redshift suppresses low redshift star formation and increases the efficacy of high redshift stellar feedback compared to the Illustris model (see Pillepich et al. 2018a). It is therefore likely that the suppressed low redshift star formation causes the downtick of $\alpha_{\rm min}$ values at low-z as well as the large uncertainty on $\alpha_{\rm min}$ at $z = 0$. The lack of evolution in $\alpha_{\rm min}$ at higher redshifts may be a feature of the increased efficacy of stellar feedback at these higher redshifts. As such, features of $\alpha_{\rm min}$ are likely sensitive to details of the wind implementation/strength prescribed by the model on which it is built (see Section 4.3 for more discussion on this).

Our result in EAGLE indicating significant redshift evolution seemingly contradicts a previous study finding the FMR is in place and does not evolve out to $z \approx 5$ in EAGLE (De Rossi et al. 2017). There is a subtle difference in the analysis between the two works, however: De Rossi et al. (2017) do not parameterise the FMR to test $\alpha_{\rm min}$ variations. They qualitatively examine the secondary dependence within the MZR and show that a M_*–$Z_{\rm gas}$–SFR relation exists at $z = 0 - 5$. This is in agreement with our results here. Consistent with De Rossi et al. (2017), we find that an $M_*-Z_{\rm gas}-$SFR relation at $z = 0 - 5$ exists in EAGLE via non-zero $\alpha_{\rm min}$ values. Despite the persistence of the M_*–$Z_{\rm gas}$–SFR relation, we find that there is some evolution through $z = 0 - 5$ in EAGLE by using the M10 projection of the FMR. It should be noted that the uncertainty of the $z = 0$ and $z = 5$ values do overlap in EAGLE. The subtly of the redshift evolution may therefore be difficult to detect without specifically fitting each redshift independently.

Overplotted on Figure 2 (gray squares) are three observationally determined values of $\alpha_{\rm min}$ from M10 (0.32), Andrews & Martini (2013; 0.66), and Curti et al. (2020; 0.55). Each of these values was determined using SDSS galaxies at $z \approx 0$ (offset horizontally for clarity). Deviations in the observational values are attributed primarily to: (i) different metallicity calibrations, (ii) using individual galaxies versus galaxy stacks (as in Andrews & Martini 2013), and (iii) selection biases towards higher star forming galaxies. Simulations are not directly effected by metallicity calibrations in the same way as observations. The sample selection criteria (outlined in Section 2.4) should help mitigate the effect of selection function biases of observations. Though we select star-forming galaxies, we do not just select the highest star forming galaxies. In spite of these potential differences, it is worth noting that the M10 $\alpha_{\rm min}$ value agrees fairly well with the TNG and Illustris derived values at $z = 0$. Although the uncertainty on the TNG $\alpha_{\rm min}$ is significant enough to include the Curti et al. (2020) value by a factor of ~1.5 times higher. Similarly, the Andrews & Martini (2013) value of 0.66 agrees fairly well with the derived value from EAGLE at $z = 0$, though we caution that this analysis was done with galaxy stacks whereas we us individual galaxies here.

4 DISCUSSION

4.1 Implications of $\alpha_{\rm min}$ variations

The derived $\alpha_{\rm min}$ values have some non-negligible redshift evolution, as was shown in the previous section. We now look at the impact of not assuming a strong FMR by examining the scatter about each of

[4] While we show in Garcia et al. (2024) this for the *stellar* metallicities, we also show in that paper that stellar and gas-phase metallicities are proportional to each other (see Section 4.1 of that work). Therefore, the same physical mechanism suppressing the correlated scatter for stellar metallicities is likely what is suppressing $\alpha_{\rm min}$ for the gas-phase as well. We note, however, that it is probable that the causality is in the opposite direction as described above.

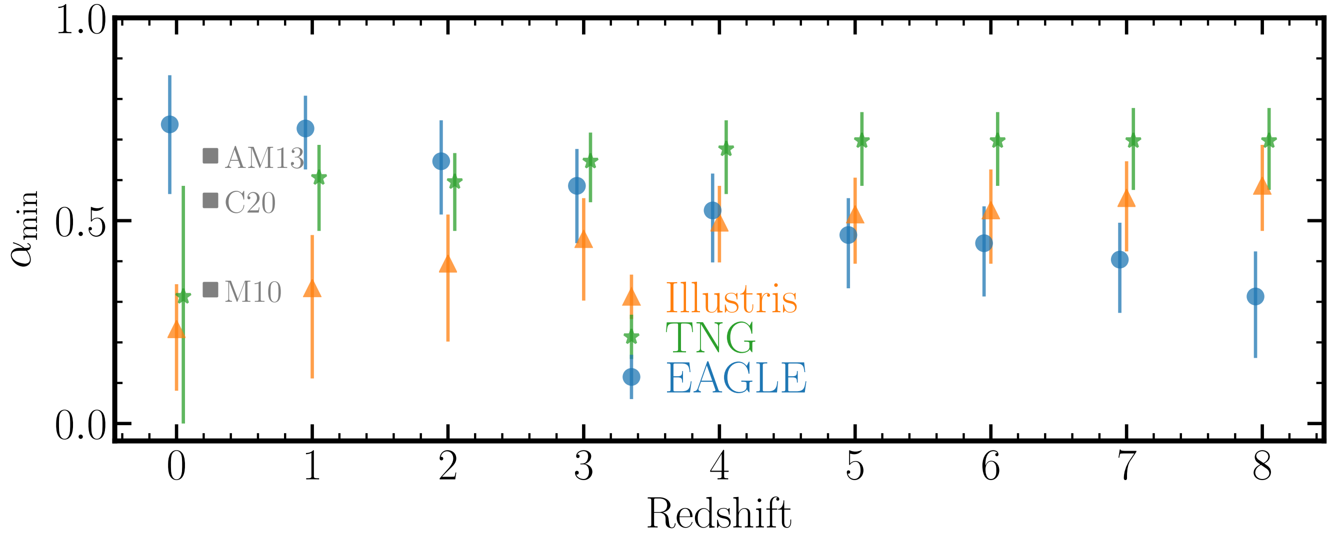

Figure 2. $\alpha_{\rm min}$ **values as a function of redshift in Illustris, TNG, and EAGLE.** $\alpha_{\rm min}$ values as a function of redshift are plotted as orange triangles, green stars, and blue circles for Illustris, TNG, and EAGLE, respectively. The errorbars here are obtained by finding α values that reduce the scatter to within 5% that of the minimized scatter. The gray squares are observational values of $\alpha_{\rm min}$ from M10, Andrews & Martini (2013), and Curti et al. (2020) determined at $z \approx 0$ via SDSS (offset from $z = 0$ for aesthetic purposes).

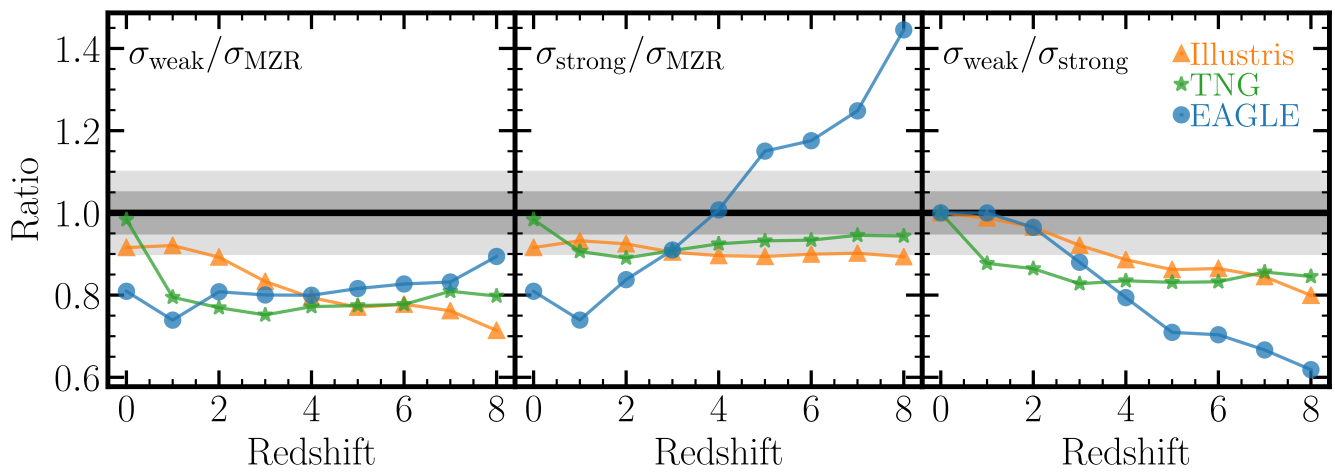

Figure 3. Reduction in scatter for weak FMR versus MZR, strong FMR vs MZR, and weak FMR versus strong FMR. *Left:* the scatter about the FMR by fitting $\alpha_{\rm min}$ at each redshift individually ($\sigma_{\rm weak}$) divided by the scatter in the MZR at each redshift ($\sigma_{\rm MZR}$) as a function of redshift. The dark and light gray shaded regions (in all panels) represent 5% and 10% variations, respectively, of each ratio. *Centre:* Same as left, but now the numerator is the scatter about the FMR evaluated in each redshift bin with a $z = 0$ calibrated $\alpha_{\rm min}$ ($\sigma_{\rm strong}$). *Right:* Previous two panels divided by each other, the reduction in scatter in the relationship by determining $\alpha_{\rm min}$ at each redshift independently ($\sigma_{\rm weak}$) divided by using the $z = 0$ $\alpha_{\rm min}$ value ($\sigma_{\rm strong}$).

these relations. Figure 3 illustrates three different ratios we examine to assess scatter reduction efficacy. We consider how the assumption of a weak FMR does compared to the MZR as a baseline. The left panel of Figure 3 shows the standard deviation of the residuals about each redshift's weak FMR normalised by that of the MZR as a function of redshift ($\sigma_{\rm weak}/\sigma_{\rm MZR}$). We find for all redshifts across the three simulations that the weak FMR reduces the scatter by $\sim 10-30\%$ compared to the MZR. The exception is TNG at $z = 0$ having scatter reduction of less than 5% – falling within the nominal uncertainty on $\alpha_{\rm min}$ and implying there is functionally no difference between the scatter of the MZR and FMR at this redshift. This $z = 0$ TNG exception was discussed previously in the context of the $\alpha_{\rm min}$ value (see Section 3.1) and the lack of a relation was attributed to the redshift scaling winds in the TNG model (see Pillepich et al. 2018a). The scatter reduction is roughly constant as a function of redshift in both TNG and EAGLE at around $\sim 20\%$ (barring the aforementioned TNG exception). Scatter reduction in Illustris ranges from 10% at $z = 0$ to nearly 30% at $z = 8$.

Next, we examine the implications of assuming a strong FMR. We define the strong FMR fit analogously to observations: we use the $z = 0$ determined $\alpha_{\rm min}$ value. We then evaluate the scatter at each redshift compared to that of the MZR at that redshift ($\sigma_{\rm strong}/\sigma_{\rm MZR}$;

middle panel Figure 3). In TNG, we find a similar trend to that of $\sigma_{\rm weak}/\sigma_{\rm MZR}$: a roughly constant scatter reduction as a function of redshift, albeit at a reduced value of ~5 – 10% (see previous discussion about the exception at $z = 0$). The scatter reduction in Illustris is similarly constant around 10%. Evidently, the redshift evolution in Illustris seen previously with $\sigma_{\rm weak}/\sigma_{\rm MZR}$ disappears when assuming a strong FMR. $\sigma_{\rm strong}/\sigma_{\rm MZR}$ actually *increases* nearly monotonically in EAGLE as a function of redshift: the strong FMR fit on the low redshift bins is significantly better than the highest redshifts. Remarkably, assuming a strong FMR actually begins to increase the scatter by 10 – 40% compared to the MZR at high redshift ($z > 5$) in EAGLE.

Finally, we show the ratio of the scatter by assuming a weak FMR divided by the scatter by assuming a strong FMR evaluated at each redshift ($\sigma_{\rm weak}/\sigma_{\rm strong}$; right panel of Figure 3). The ratio $\sigma_{\rm weak}/\sigma_{\rm strong}$ is of particular interest as it provides a diagnostic for how well an assumed strong FMR characterises galaxies at higher redshift compared to their minimum scatter projection. The ratio is unity at $z = 0$ by construction since the strong FMR assumes the $z = 0$ $\alpha_{\rm min}$ value at for all redshifts. In Illustris and EAGLE at $z \leq 2$ the scatter reduction by assuming a strong fit is less than 5% (within our uncertainty on $\alpha_{\rm min}$). The relatively low decrease in the scatter implies that the strong FMR might hold (or be approximately true) at these low redshift (qualitatively consistent with previous observational findings; M10; Cresci et al. 2019). The scatter reduction at $z \geq 3$, however, is $\gtrsim 10$%. Both Illustris and EAGLE have monotonically decreasing ratios of scatter in the high-z regime out to a 20% decrease in Illustris and nearly 40% in EAGLE. The scatter reduction stays roughly constant in TNG at just over 10% at $z > 0$. This roughly constant scatter reduction lends further credence to the idea that there is little redshift evolution of the FMR in TNG at any redshift *but* $z = 0$. The decrease in scatter when assuming a weak FMR indicates that high redshift galaxies are different from the low redshift systems. The strong FMR hypothesis clearly does not effectively characterise higher redshift galaxies. This marked shift in efficacy of the strong FMR indicates that there is some time evolution within the FMR past $z \geq 3$ in Illustris and EAGLE.

In summary, by determining $\alpha_{\rm min}$ at each redshift independently we find that at $z \gtrsim 3$ the scatter can be reduced an additional ~ 10 – 35% compared to an assumed strong FMR. We therefore conclude that the variations in $\alpha_{\rm min}$ are significant past this redshift Significant variations past $z \gtrsim 3$ seem to imply that the strong FMR is not even a good approximation in the early universe.

4.2 Advantages and Challenges of a weak FMR Framework

The key advantage of fitting each redshift independently is to more effectively minimize the scatter. The weak FMR gives us a clear-cut metric for the strength of the MZR's secondary dependence on SFR arises that is completely independent of the evolution of the normalisation of the MZR. Independence from other redshift populations removes the possibility of conflating evolution of the normalisation of the MZR with evolution of the scatter. By assuming a strong FMR we suppress any variations of $\alpha_{\rm min}$ as a function of redshift. As a consequence, the strong FMR does not optimally reduce scatter across redshift (discussed in more detail in Section 4.1). Using a weak FMR assumption therefore allows a more careful examination for the extent to which the observed FMR has variations. If evolution exist and $\alpha_{\rm min}$ does not vary, it can be concluded that evolution *must* be driven by the evolution of the normalisation of the MZR.

A challenge of performing a similar analysis in observations is the amount of data available. Lower redshift galaxy populations are well sampled, but at higher redshift sampling becomes more difficult. It is possible that subtle changes can be measured at lower redshifts (see Pistis et al. 2023 for a potential detection at $z \sim 0.63$); however, the most significant evolution in $\alpha_{\rm min}$ happens in these highest redshift populations (Figure 2). More complete samples of galaxy populations at these early times with, e.g., JWST are therefore required in order to undergo any weak FMR-style analysis to detect significant deviations from the $z = 0$ $\alpha_{\rm min}$ values. Moreover, a redshift-complete sample would be limited by our understanding of metallicity in the high redshift universe. Recently, work has been done to obtain reliable metallicity diagnostics at $z > 4$ using *JWST*/NIRSpec (e.g., Nakajima et al. 2023; Sanders et al. 2023; Shapley et al. 2023). However, more complete galaxy samples are required, particularly at the low metallicities seen at this epoch, to fully characterise these diagnostics. As such, it would be difficult to ensure that $\alpha_{\rm min}$ values determined observationally are fair comparisons across the broad redshift range examined in this work.

4.3 Dependence on small scale physics implementations

We find that in each of these three models there exists a weak FMR. The $\alpha_{\rm min}$ values are not the same, nor do they evolve in the same fashion, in the different models, however. The value of $\alpha_{\rm min}$ at any given redshift is a complicated by-product of a number of different physical processes. While we have some qualitative understanding of how $\alpha_{\rm min}$ is set (or changed), the exact mechanisms $\alpha_{\rm min}$ are not entirely clear in detail.

What is clear is that $\alpha_{\rm min}$ is sensitive to the physics driving galaxy evolution. For example, in Section 3.1, we attributed the lowered $\alpha_{\rm min}$ values in TNG at $z = 0$ to the redshift-dependent wind prescription in the TNG model (as mentioned in Section 3.1). Through this example, the sensitivity of $\alpha_{\rm min}$ to the input physics within the simulation models becomes clear. The redshift-dependent winds in TNG work to increase wind velocities at low redshift which suppresses star formation. This star formation suppression likely plays a significant role in the overall decrease of $\alpha_{\rm min}$ seen at low redshifts in TNG.

All three models examined here rely on effective equation of state sub-grid models for the dense, unresolved ISM (Springel & Hernquist 2003 for Illustris/TNG and Schaye & Dalla Vecchia 2008 for EAGLE). In recent years, however, high-resolution simulation modelling has begun to directly resolve the sites of star formation (e.g., Feedback In Realisitc Environments model; Hopkins et al. 2014). The stellar feedback in such simulations is much burstier than in the models presented here. We believe that bursty stellar feedback events should suppress $\alpha_{\rm min}$ values compared to Illustris, TNG, and EAGLE. The bursty stellar feedback is a result of burstier star formation histories, wherein star formation occurs over a much shorter period of time. Bursts may therefore curtail the effectiveness of star formation rates in regulating the gas-phase metallicity of a galaxy. Therefore the redshift variations $\alpha_{\rm min}$ profile may be able to provide constraining power on the extent to which galaxies' feedback is more bursty or smooth. Although it should be noted that even within these smooth feedback models there is some disparity.

5 CONCLUSIONS

We select central star forming galaxies with stellar mass $8.0 < \log(M_* \ [M_\odot]) < 12.0$ with gas mass $\log(M_{\rm gas} \ [M_\odot]) > 8.5$ from $z = 0 - 8$ in the cosmological simulations Illustris, IllustrisTNG, and EAGLE. We investigate the extent to which the M10 parameterisation of the fundamental metallicity relation (FMR; Equation 1) holds. The parameter of merit in the M10 parameterisation is $\alpha_{\rm min}$, which traditionally is understood as a parameter to minimize scatter about the MZR. Physically, $\alpha_{\rm min}$ sets a projection direction of the mass-metallicity-SFR space to a 2D space with minimal scatter. Many observational studies have claimed that this projection direction does not evolve with redshift (Mannucci et al. 2010; Cresci et al. 2019). This potentially indicates that the FMR can predict the evolution of both the scatter about the MZR and the normalisation of the MZR.

We define both a strong and weak FMR hypothesis. In the context of this work, the strong FMR hypothesis implies that $\alpha_{\rm min}$ does not change as a function of redshift where as the weak FMR hypothesis states the opposite. More generally, the strong FMR hypothesis states the the M10 parameterisation can describe both the scatter and noramlisation of the MZR at the same time.

Our conclusions are as follows:

- We find that there is non-negligible evolution of the strength of the MZR's secondary correlation with SFR as a function of redshift (Figure 2). This result suggests that the strong FMR hypothesis does not hold in Illustris, TNG, and EAGLE.
- We find that the weak FMR ($\alpha_{\rm min}$ determined at each redshift independently) consistently reduces scatter around $10-30\%$ compared to the the MZR (left panel of Figure 3). The strong FMR also reduces the scatter compared to the MZR, albeit to a lesser extent than the weak FMR. At high-z in EAGLE, however, using the strong FMR actually *increases* scatter compared to the MZR (centre panel of Figure 3). Overall, we find that at $z \gtrsim 3$ fitting galaxies with a weak FMR can reduce scatter $\sim 5-40\%$ more than using the strong FMR (right panel of Figure 3).

Obtaining one relationship that describes the metal evolution of all galaxies across time is an ambitious goal. It is worth appreciating how reasonably well a simple linear combination of two parameters can begin to achieve that goal at low redshift. Yet it is not perfect. The results from this work show that Illustris, TNG, and EAGLE indicate deviations from the strong FMR hypothesis. It is presently unclear whether the same is true in observations. Understanding whether the FMR in observations is weak or strong will aid in being able to understand the recent *JWST* observations suggesting high redshift FMR evolution.

ACKNOWLEDGEMENTS

AMG acknowledges Carol, Kate, and Kelly Garcia for assistance in the design of Figure 1. We acknowledge the Virgo Consortium for making their simulation data available. The EAGLE simulations were performed using the DiRAC-2 facility at Durham, managed by the ICC, and the PRACE facility Curie based in France at TGCC, CEA, Bruyèresle-Châtel.

KG is supported by the Australian Research Council through the Discovery Early Career Researcher Award (DECRA) Fellowship (project number DE220100766) funded by the Australian Government. KG is supported by the Australian Research Council Centre of Excellence for All Sky Astrophysics in 3 Dimensions (ASTRO 3D), through project number CE170100013.

DATA AVAILABILITY

The reduced data products, analysis scripts, and figures are all available publicly at https://github.com/AlexGarcia623/Does-the-FMR-evolve-Simulations/. Data from Illustris and IllustrisTNG is publicly available on each project's respective website. Illustris: https://www.illustris-project.org/data/ and IllustrisTNG: https://www.tng-project.org/data/. Similarly, data products from the EAGLE simulations are available for public download via the Virgo consortium's website: https://icc.dur.ac.uk/Eagle/database.php

REFERENCES

Andrews B. H., Martini P., 2013, ApJ, 765, 140
Belli S., Jones T., Ellis R. S., Richard J., 2013, ApJ, 772, 141
Blanc G. A., Lu Y., Benson A., Katsianis A., Barraza M., 2019, ApJ, 877, 6
Bothwell M. S., Maiolino R., Kennicutt R., Cresci G., Mannucci F., Marconi A., Cicone C., 2013, MNRAS, 433, 1425
Bothwell M. S., Maiolino R., Peng Y., Cicone C., Griffith H., Wagg J., 2016, MNRAS, 455, 1156
Chabrier G., 2003, PASP, 115, 763
Crain R. A., et al., 2015, MNRAS, 450, 1937
Cresci G., Mannucci F., Curti M., 2019, A&A, 627, A42
Curti M., Mannucci F., Cresci G., Maiolino R., 2020, MNRAS, 491, 944
Curti M., et al., 2023, arXiv e-prints, p. arXiv:2304.08516
Dalcanton J. J., 2007, ApJ, 658, 941
Davé R., Finlator K., Oppenheimer B. D., 2011, MNRAS, 416, 1354
Davis M., Efstathiou G., Frenk C. S., White S. D. M., 1985, ApJ, 292, 371
Dayal P., Ferrara A., Dunlop J. S., 2013, MNRAS, 430, 2891
De Rossi M. E., Theuns T., Font A. S., McCarthy I. G., 2015, MNRAS, 452, 486
De Rossi M. E., Bower R. G., Font A. S., Schaye J., Theuns T., 2017, MNRAS, 472, 3354
De Rossi M. E., Bower R. G., Font A. S., Schaye T., 2018, Boletin de la Asociacion Argentina de Astronomia La Plata Argentina, 60, 121
Dolag K., Borgani S., Murante G., Springel V., 2009, MNRAS, 399, 497
Donnari M., et al., 2019, MNRAS, 485, 4817
Ellison S. L., Patton D. R., Simard L., McConnachie A. W., 2008, ApJ, 672, L107
Elmegreen B. G., 1999, ApJ, 527, 266
Fontanot F., et al., 2021, MNRAS, 504, 4481
Garcia A. M., et al., 2023, MNRAS, 519, 4716
Garcia A. M., et al., 2024, arXiv e-prints, p. arXiv:2401.12310
Genel S., et al., 2014, MNRAS, 445, 175
Heintz K. E., et al., 2023, Nature Astronomy, 7, 1517
Hemler Z. S., et al., 2021, MNRAS, 506, 3024
Hopkins P. F., Kereš D., Oñorbe J., Faucher-Giguère C.-A., Quataert E., Murray N., Bullock J. S., 2014, MNRAS, 445, 581
Kewley L. J., Nicholls D. C., Sutherland R. S., 2019, ARA&A, 57, 511
Koeppen J., 1994, A&A, 281, 26
Lacey C. G., Fall S. M., 1985, ApJ, 290, 154
Langeroodi D., Hjorth J., 2023, arXiv e-prints, p. arXiv:2307.06336
Langeroodi D., et al., 2023, ApJ, 957, 39
Lara-López M. A., et al., 2010, A&A, 521, L53
Lee H., Skillman E. D., Cannon J. M., Jackson D. C., Gehrz R. D., Polomski E. F., Woodward C. E., 2006, ApJ, 647, 970
Lilly S. J., Carollo C. M., Pipino A., Renzini A., Peng Y., 2013, ApJ, 772, 119
Looser T. J., D'Eugenio F., Piotrowska J. M., Belfiore F., Maiolino R., Cappellari M., Baker W. M., Tacchella S., 2024, arXiv e-prints, p. arXiv:2401.08769
Maiolino R., et al., 2008, A&A, 488, 463
Mannucci F., Cresci G., Maiolino R., Marconi A., Gnerucci A., 2010, MNRAS, 408, 2115
Marinacci F., et al., 2018, MNRAS, 480, 5113
McAlpine S., et al., 2016, Astronomy and Computing, 15, 72
Naiman J. P., et al., 2018, MNRAS, 477, 1206
Nakajima K., Ouchi M., Isobe Y., Harikane Y., Zhang Y., Ono Y., Umeda H., Oguri M., 2023, ApJS, 269, 33
Nelson D., et al., 2018, MNRAS, 475, 624
Nelson D., et al., 2019a, Computational Astrophysics and Cosmology, 6, 2

Nelson D., et al., 2019b, MNRAS, 490, 3234
Nelson E. J., et al., 2021, MNRAS, 508, 219
Pillepich A., et al., 2018a, MNRAS, 473, 4077
Pillepich A., et al., 2018b, MNRAS, 475, 648
Pillepich A., et al., 2019, MNRAS, 490, 3196
Pistis F., et al., 2023, arXiv e-prints, p. arXiv:2312.00930
Salim S., Lee J. C., Davé R., Dickinson M., 2015, ApJ, 808, 25
Sanders R. L., et al., 2015, ApJ, 799, 138
Sanders R. L., et al., 2018, ApJ, 858, 99
Sanders R. L., et al., 2021, ApJ, 914, 19
Sanders R. L., Shapley A. E., Topping M. W., Reddy N. A., Brammer G. B., 2023, arXiv e-prints, p. arXiv:2303.08149
Savaglio S., et al., 2005, ApJ, 635, 260
Schaye J., 2004, ApJ, 609, 667
Schaye J., Dalla Vecchia C., 2008, MNRAS, 383, 1210
Schaye J., et al., 2015, MNRAS, 446, 521
Shapley A. E., Reddy N. A., Sanders R. L., Topping M. W., Brammer G. B., 2023, arXiv e-prints, p. arXiv:2303.00410
Somerville R. S., Davé R., 2015, ARA&A, 53, 51
Springel V., 2005, MNRAS, 364, 1105
Springel V., 2010, MNRAS, 401, 791
Springel V., Hernquist L., 2003, MNRAS, 339, 289
Springel V., White M., Hernquist L., 2001, ApJ, 549, 681
Springel V., et al., 2018, MNRAS, 475, 676
Torrey P., Vogelsberger M., Genel S., Sijacki D., Springel V., Hernquist L., 2014, MNRAS, 438, 1985
Torrey P., et al., 2018, MNRAS, 477, L16
Tremonti C. A., et al., 2004, ApJ, 613, 898
Vogelsberger M., Genel S., Sijacki D., Torrey P., Springel V., Hernquist L., 2013, MNRAS, 436, 3031
Vogelsberger M., et al., 2014a, MNRAS, 444, 1518
Vogelsberger M., et al., 2014b, Nature, 509, 177
Weinberger R., et al., 2017, MNRAS, 465, 3291
Wiersma R. P. C., Schaye J., Theuns T., Dalla Vecchia C., Tornatore L., 2009, MNRAS, 399, 574
Wuyts E., Rigby J. R., Sharon K., Gladders M. D., 2012, ApJ, 755, 73
Yang N., Scholte D., Saintonge A., 2024, MNRAS, 527, 11043
Zahid H. J., Kewley L. J., Bresolin F., 2011, ApJ, 730, 137
Zahid H. J., Dima G. I., Kudritzki R.-P., Kewley L. J., Geller M. J., Hwang H. S., Silverman J. D., Kashino D., 2014, ApJ, 791, 130

APPENDIX A: (LACK OF) DEPENDENCE ON SPECIFIC STAR FORMATION MAIN SEQUENCE

Part of our galaxy selection criteria (see Section 2.4 for full details) includes selecting star forming galaxies. Our method of doing so uses a specific star formation main sequence cut. The sSFMS selection includes a cut excluding galaxies 0.5 dex below the median relation. In this appendix, we consider three additional variations on this cut (following from Garcia et al. 2024): (i) a more restrictive cut of all galaxies 0.1 dex below the median relation, (ii) a less restrictive cut of all galaxies 1.0 dex below the median relation, and (iii) a very liberal cut of all galaxies with non-zero SFRs. We show the resultant $\alpha_{\rm min}$ values from these cuts in Figure A1. The uncertainty bars on $\alpha_{\rm min}$ overlap for all redshift bins in all three analysed simulations with all four cuts. However, there are three cases in which the derived $\alpha_{\rm min}$ value itself varies significantly for the SFR > 0 cut: TNG $z = 1$ and 2 as well as EAGLE $z = 0$. In these three cases, $\alpha_{\rm min}$ is significantly offset from the errorbars of at least two of the three other cuts. The uncertainties using the SFR > 0 cut in these three cases are quite large. This suggests that the overall change in scatter when using the SFR > 0 cut versus another cut is marginal. We therefore conclude that, while the derived $\alpha_{\rm min}$ value may change, these changes have no qualitative bearing on the results presented in this work.

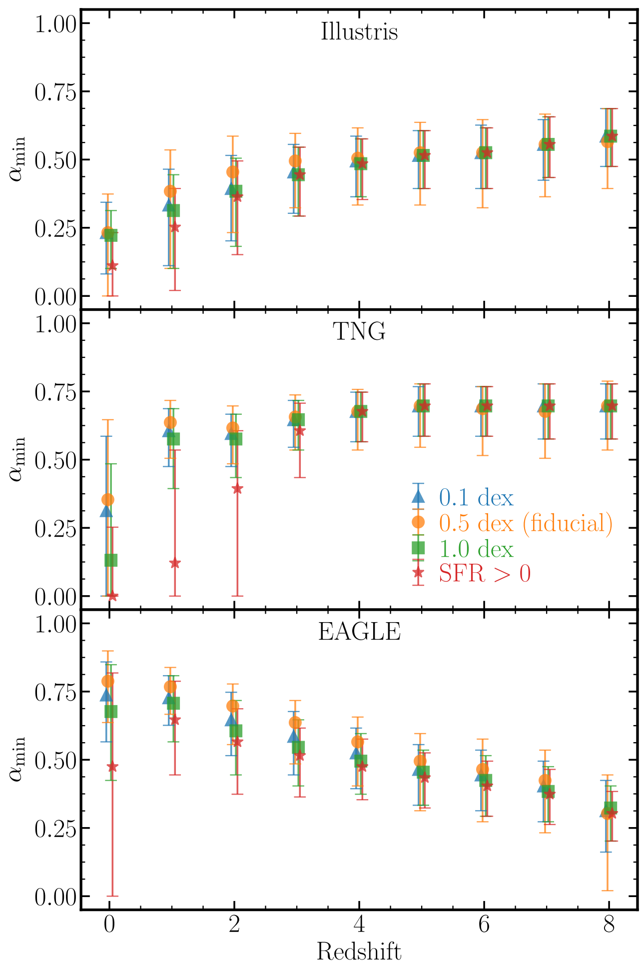

Figure A1. Determination of $\alpha_{\rm min}$ as a function of redshift for Illustris (top), TNG (centre), and EAGLE (bottom) for the four different sSFMS variations.

APPENDIX B: HIGHER ORDER POLYNOMIAL FIT

M10 determined residuals in the scatter about a fourth-order polynomial instead of a linear regression. This practice is not consistent through all works using the μ_α 2D projection of the FMR, however. For example, recent *JWST* observational papers (e.g., Nakajima et al. 2023; Langeroodi & Hjorth 2023) adopt a linear regression definition of the FMR from Andrews & Martini (2013). We show that using a linear regression does not significantly change the projection of least scatter in Illustris, TNG, and EAGLE in Figure B1.

This paper has been typeset from a TEX/LATEX file prepared by the author.

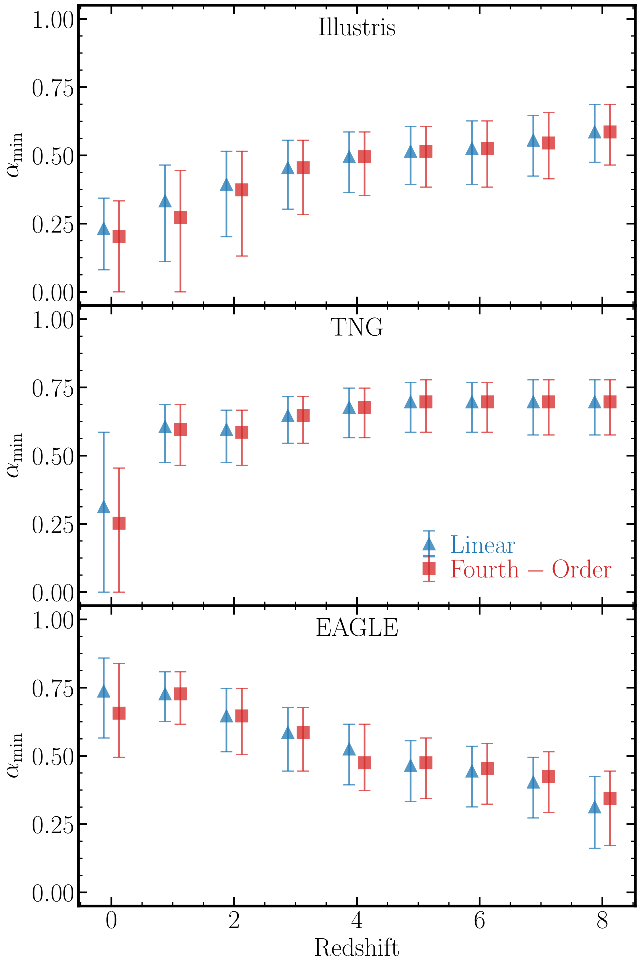

Figure B1. Determination of $\alpha_{\rm min}$ as a function of redshift for Illustris (top), TNG (centre), and EAGLE (bottom) using a linear regression (blue triangles) and fourth-order polynomial regression (red squares).